Journal of Instrumentation

SISSA

PAPER

Time encoded imaging of extended gamma-ray sources in 3D using the OrionUM pixelated CdZnTe with subpixel estimation and depth of interaction corrections

To cite this article: D. Shy *et al* 2021 *JINST* **16** P03013

Jinst

Published by IOP Publishing for Sissa Medialab

Received: *November 1, 2020*
Revised: *December 13, 2020*
Accepted: *January 4, 2021*
Published: *March 8, 2021*

Time encoded imaging of extended gamma-ray sources in 3D using the OrionUM pixelated CdZnTe with subpixel estimation and depth of interaction corrections

D. Shy,[a,*] **M. Petryk,**[a] **Z. Chen,**[a] **S. Thompson**[b] **and Z. He**[a]

[a] *Nuclear Engineering and Radiological Sciences, University of Michigan, 2355 Bonisteel Blvd, Ann Arbor, MI 48109, U.S.A.*
[b] *Nuclear Nonproliferation Division, Idaho National Laboratory, 2351 N. Boulevard, Idaho Falls, ID 83402, U.S.A.*

E-mail: danielshy@danielshy.com

Abstract: Nuclear holdup, or the accumulation of material in processing equipment, is important to localize, identify, and quantify for economic reasons and criticality safety. As a part of the quantification process is to estimate the geometric distribution of the material, high-resolution 3D images are desired. To image gamma-ray material in 3D, we propose a time-encoded imaging technique that uses a mobile coded aperture to modulate the gamma-ray signal spatially and temporally. In the process, we investigate means to improve upon the image resolution. Naturally, the quality of the reconstructed image is dependent on the size of the aperture and the fidelity of the recorded projection, among other factors. The major degradation in the recorded projection originates from the poor position reconstruction of the gamma-ray interaction location within the detector. By utilizing the subpixel capabilities of the OrionUM pixelated CdZnTe system, the position of each gamma interaction can be estimated with a resolution of 500 µm full-width-at-half-maximum (FWHM) for a 120 keV gamma ray. With subpixel estimation, the average FWHM of a double-Gaussian fit improves by almost 10% when imaging two ^{57}Co sources placed 1 cm apart. Next, by applying a collimator verified depth of interaction correction scheme, the image resolution improves by 7.5% and 12.3% for the FWHM and the full-width-at-tenth-maximum respectively for the studied source configuration. Finally, the estimation of the 3D distribution of a gamma-ray source is demonstrated via a depth refocusing technique. This technique is shown on spatially extended special nuclear material measured at Idaho National Laboratory and estimates the material's out of plane angle to within 20% of the true angle.

Keywords: Gamma camera, SPECT, PET PET/CT, coronary CT angiography (CTA); Gamma detectors (scintillators, CZT, HPGe, HgI etc); Inspection with gamma rays

*Corresponding author.

https://doi.org/10.1088/1748-0221/16/03/P03013

2021 JINST 16 P03013

Contents

1 Introduction

Coded aperture imaging is a technique to image radiation particles and has applications in astronomy [1], medicine [2], and homeland security [3]. The coded aperture mask spatially encodes the radiation source. Then, the image is reconstructed from the projected shadow cast on the radiation detector. This presents an attractive approach to image low-energy gamma rays ($< 250\,\text{keV}$) with pixelated CdZnTe [4], as the main mode of gamma-matter interaction in that energy range is photoelectric absorption.

Time-encoded imaging (TEI) is an extension of coded aperture imaging, in that it uses a coded aperture to spatially encode the source, but also contains a temporal encoding component [5, 6]. It can be accomplished via a space-and-time changing mask [7], self modulation [8], or a mobile coded mask [9].

Mapping of radiological material in 3D allows for spatial quantification and has applications in nuclear material holdup, or the accumulation of nuclear material in processing equipment such as pipes. There, the operator requires both the knowledge of the source location and amount in that location for purposes of radiation safety and accountability. Traditionally, holdup is estimated via gamma-ray spectroscopy and collimation around the region of interest. One quantification technique is accomplished via the use of the Generalized Geometry Holdup model [10]. There, the object of interest is generalized to a point, line, or plane and is then used in an analytical model along with the gamma-ray measurement to estimate the quantity of material. False or biased geometric assumptions can result in poor outcomes. Rebei et al. investigated the possible bias due to geometry error and report an up to 30% underestimation of source mass for the studied configuration [11].

2021 JINST 16 P03013

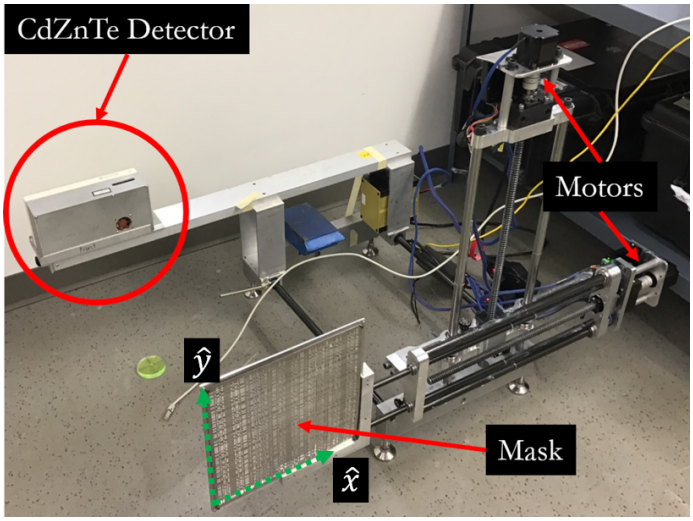

Figure 1. The OrionUM CdZnTe detector attached to the Mira system with the tungsten coded mask and the stepper motors labeled. Green dashed arrows depict the $\hat{x}$ and $\hat{y}$ coordinate system as well as the direction of motion of the mask and that of the image space.

They also propose a 3D imaging technique via a series of detector arrays surrounding the object of interest for geometry estimation to reduce the error on the estimated activity.

This manuscript presents work on imaging spatially extended gamma-ray sources in 3D using a depth-refocusing technique that TEI exhibits. In the process, we present advancements in the University of Michigan's 'Mira' TEI system to maximize the potential of the imaging process. The first improvement is accomplished by leveraging the digital OrionUM system, which can provide the subpixel location of each interaction. Next, improvements in image resolution are accomplished by the application of depth-of-interaction corrections that are verified with collimator experiments. Section 2 summarizes the systems employed in the study. Section 3 discusses the additions of sub-pixel and the depth of interaction corrections. Section 4 presents 3D source distribution estimation via a depth-refocusing technique. Although the depth-refocusing technique was previously used by Brown et al. [6], we expand the technique and demonstrate it for extended sources distributed in 3 dimensions. This work is concluded with the 3D estimation of spatially extended special nuclear material from an experiment conducted at Idaho National Laboratory (INL).

2 Systems employed in study

The TEI system is comprised of a 3D position-sensitive CdZnTe gamma-ray detector as well as the 'Mira' system that translates the coded mask in a manner such that the detector is in the umbra of the coded shadow. Figure 1 depicts the imaging-detector system.

2.1 The University of Michigan OrionUM pixelated CdZnTe detector system

The OrionUM [12] system is composed of nine $2 \times 2 \times 1.5\,\text{cm}^3$ CdZnTe crystals arranged in a $3 \times 3 \times 1$ array with the planar cathodes facing towards the source. There is a 0.5 cm space between each crystal when arranged in the array. Each crystal, which we will refer to as a module, has an

2021 JINST 16 P03013

11×11 pixelated anode array with a 1.72 mm pitch and a planar cathode. The energy resolution of the detector is better than 0.35% FWHM at 662 keV for single-pixel events [13].

The depth of interaction is estimated via the cathode-to-anode ratio for single pixel events [14]. It has consistently shown a depth resolution better than 1 mm FWHM at 662 keV [15]. The OrionUM system is also capable of subpixel localisation of the gamma-ray interaction [16]. The subpixel estimation technique relies on the Shockley-Ramo principle of charge induction that governs the relationship between the various induced charge profiles and the trajectory of the charge carriers relative to the collecting electrode [14, 17, 18]. Therefore, monitoring the transient signal on the neighboring pixels will reveal the subpixel location by using a weighted sum approach. We do this by implementing a 'trigger-plus-8' mode, where the triggered pixel is read out along with the eight surrounding pixels.

Equation (2.1) outlines the calculation for the column and row summation and uses a 3×3 matrix to denote the triggered and 8 surrounding pixels. The individual elements s_{ij} are the signal amplitudes of the pixel at the ith row and the jth column. With the center element (s_{22}) denoting the triggered pixel, s_{left} and s_{right} represent the left and right column summation of the pixel relative to the triggered pixel while s_{top} and s_{bottom} represent the top and bottom rows. The rows and column signal summations can be processed as

$$\begin{aligned} s_{\text{left}} &= s_{11} + s_{21} + s_{31} \\ s_{\text{right}} &= s_{13} + s_{23} + s_{33} \\ s_{\text{top}} &= s_{11} + s_{12} + s_{13} \\ s_{\text{bottom}} &= s_{31} + s_{32} + s_{33}. \end{aligned} \tag{2.1}$$

Next, (2.2) summarizes the opposing neighbouring ratio subpixel estimation technique.

$$\begin{aligned} R_x &= \frac{s_{\text{left}} - s_{\text{right}}}{s_{\text{left}} + s_{\text{right}}} \\ R_y &= \frac{s_{\text{top}} - s_{\text{bottom}}}{s_{\text{top}} + s_{\text{bottom}}}. \end{aligned} \tag{2.2}$$

This readout logic therefore allows for the subpixel estimation in the lateral and horizontal direction. Currently, the system has a 300 µm FWHM position resolution for 662 keV events and 500 µm FWHM at 120 keV [16].

2.2 Mira, the time encoding imaging system

The Mira system facilitates the movement of the mask [6]. It has two stepper motors to translate the mask horizontally and vertically, or the $\hat{x}$ and $\hat{y}$ direction (see coordinate systems in figure 1). The detector is mounted on an assembly that is held by two rails on which it can slide to vary the mask-to-detector distance. On the assembly, the detector's cathodes face the mask and can slide back to have a maximum mask-to-detector separation of 59 cm.

The coded mask is attached at the end of the horizontal arm. It is made of layered tungsten sheets, each 0.25 mm thick. The mask is a rank 79 modified uniformly redundant array (MURA) [19] with a total of 200×200 elements for a total size of 12 in $\times$ 12 in. The MURA pattern is therefore mosaicked ~2.53 times. Each element, or pixel pitch, is 1.4 mm wide with figure 2 depicting the mask.

2021 JINST 16 P03013

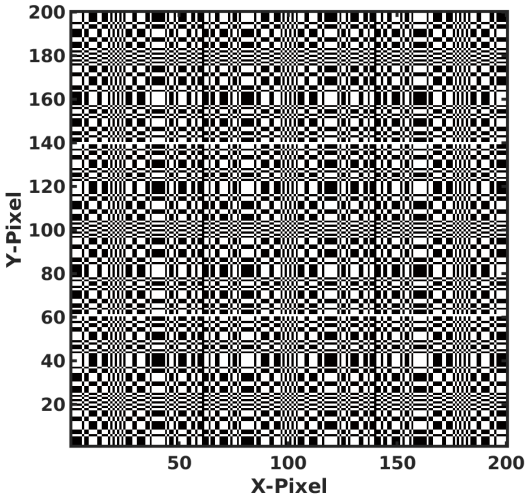

Figure 2. The 200×200 element rank 79 MURA mask that is mosaicked ~2.53 times. Black pixels represent closed elements while white pixels present open elements. The mask is a near 50% open fraction that has a mask and anti-mask relationship via a 90° rotation. However, this feature was not used in this study.

In this study, four mask sheets were used together totaling 1 mm of thickness as an optimization between attenuation and collimation effects when using thicker masks. A more detailed description of the mask and its translational system is available in [20]. Although the MURA pattern has mask-antimask properties, they were not utilized in this study.

Under normal measurement conditions, the mask would raster scan across $79 \times 79 = 6241$ elements in the $\hat{x}$ and $\hat{y}$ directions. It would first move in the $\hat{x}$ direction for a distance that is equivalent to the rank of the mask, or 11.06 cm. Following a scan of a single row continuously, the mask will translate one element in the $\hat{y}$ direction and complete another row scan in the opposite direction. This is repeated until the mask has moved through all elements of the rank 79 MURA. In the meantime, a data acquisition computer system records the gamma-ray interactions along with a timestamp to match that of the mask time tag.

3 Implementation advancements in the time-encoded imaging system

A mathematical model of the observation matrix can be formulated as follows:

$$\mathbf{O} = \mathbf{F} \star \mathbf{A} \star \mathbf{D} + \eta, \tag{3.1}$$

where $\mathbf{O}$ is the observation matrix, $\mathbf{F}$ is the unknown true source distribution, $\mathbf{A}$ is the mask transmission matrix, $\mathbf{D}$ is the detector response term, and η is the noise term. The mathematical operation ($\star$) represents a correlation operator. Correlation with a decoding function $\mathbf{G}$ presents one of the more popular reconstruction techniques [19] and is the technique used in this study:

$$\hat{\mathbf{F}} = \mathbf{O} \star \mathbf{G}, \tag{3.2}$$

with $\hat{\mathbf{F}}$ representing the estimated source distribution. $\mathbf{G}$ is chosen such that $\mathbf{G} \star \mathbf{A} = \delta$, where δ is a Kronecker delta with a 1 in the center and 0 otherwise.

2021 JINST 16 P03013

Resolution is related to the pixel pitch of the apertures and how well the projection can be recorded, specifically, the resolving of the demarcation between different mask elements. Blurring in the recorded pattern can be modeled as **D** in (3.1). If the detector were able to record the pattern with infinite resolution, **D** can then be modeled as a Kronecker delta function. If it were anything else, the point spread function is then modified by the behavior of **D**. The blurring due to **D** is related to the pixelation of the detector systems. In most circumstances, increasing the detector pixel size would increase the blur in the reconstructed images. Therefore, the addition of subpixel information should increase the fidelity of the recorded pattern and reduce the blurring in the reconstructed image due to **D**.

It also follows that the projected magnification will also affect the image as the recorded pattern is re-scaled. The magnification M_d of the projection is

$$M_d = 1 + \frac{B_d}{A}, \tag{3.3}$$

where A and B_d represent the source-to-mask and detector-to-mask distances of the dth depth bin of the detector module respectively. This implies that the projected mask pattern will vary with different depths in the CdZnTe module as it extends 1.5 cm in depth. We therefore apply a depth of interaction (DOI) correction factor, similar to that of Ziock et al. [21].

3.1 Implementation of subpixel estimation

This work uses the digital OrionUM system that is capable of superior position resolution when compared to its analog predecessor used in the original prototype of the TEI system [6, 16]. To demonstrate the benefit of implementing subpixel estimation, a 63 µCi ^{57}Co source was imaged with and without subpixel approximation. Figure 3 presents the experimental setup that measures two sources spaced 1 cm apart. Since two sources of the same activity were not available, two measurements of the same source were taken at two different times, each at a different location. Following the measurements, the data sets were added together to emulate a two source system. The source was placed near the isocenter of the detector with a source-to-mask distance of $A = 71$ cm. The detector's cathode side was facing the source and placed 30 cm away from the mask. First, an image of the top source was developed with and without subpixel estimation. For the second measurement location, the source was moved 1 cm vertically with a micro-translation stage followed by the same sequence. This was done to reduce error from moving the source repeatedly.

Note that the true geometry of the check source is unknown as the nuclear material is deposited in epoxy and cannot be assumed to be a point source. According to the manufacturer, Eckert and Ziegler, the type D disk source has an active diameter of 5 mm [22]. However, since the manufactured tolerances cannot be quantified, all reported values include the extent of the sources.

Figure 4 shows the reconstructed images with and without the application of subpixel sensing. By the first inspection, the peak-to-saddle ratio, or the region between the two peaks, is lower and allows for superior separability of the two sources. Table 1 presents the associated FWHM image metrics of the sources and shows that the FWHM has improved by almost 10% when applying subpixel sensing for the given experimental configuration. All FWHM values have a 95% confidence interval margin of error of 0.02 cm as calculated by MATLAB's 'gauss2' fitting tool and indicate that the FWHM values are not within each other's 95% interval.

2021 JINST 16 P03013

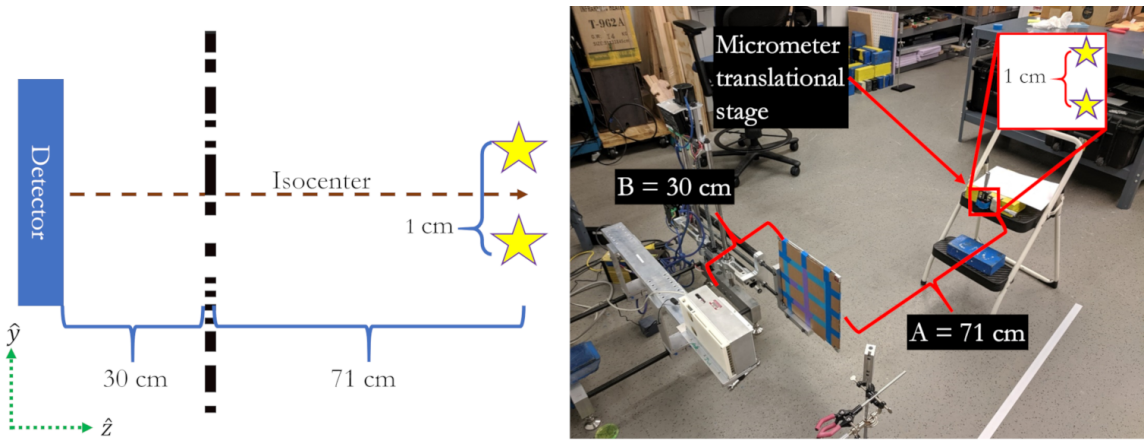

Figure 3. Setup of the experiment to demonstrate the improvements in image resolution when applying subpixel estimation. The arrangement of the sources is available in the inset image displaying the two sources positioned vertically 1 cm apart.

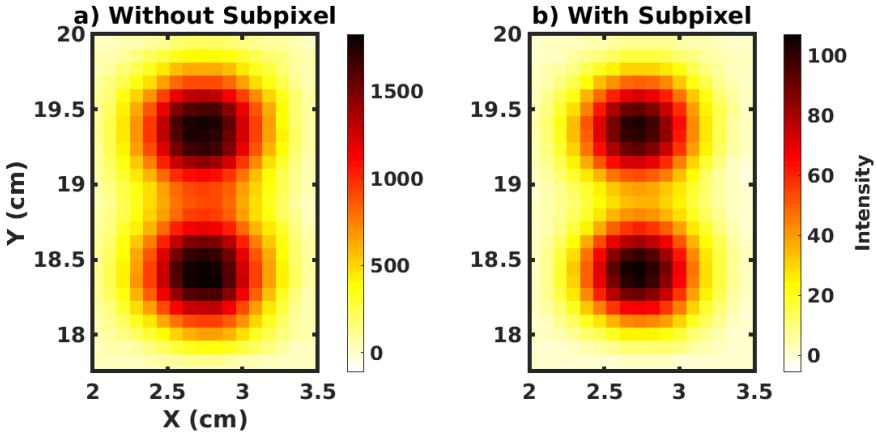

Figure 4. Reconstructed images of the two source experiment (a) without and (b) with subpixel estimation.

Table 1. Full-width-at-half-maximum values for the two source experiment as calculated via a double Gaussian fit of the vertical cross-section. It also presents the percent decrease. All width values are in centimeters. The error bounds present the 95% confidence interval on the fit's coefficients.

	FWHM Bottom	FWHM Top
Without subpixel	0.66 ± 0.02	0.64 ± 0.02
With subpixel	0.60 ± 0.02	0.58 ± 0.02
Percent decrease	9.9%	9.4%

2021 JINST 16 P03013

3.2 Depth of interaction correction

The assumption that all events occur at the cathode's surface can lead to blurring, especially at the edges of the field of view (FOV) [21]. Naturally, the image response will vary in different detector depths due to the projection magnification. To compensate for the effect, the frames of the reconstructed images are "zero-padded" based on the different magnifications they experience and then summed together. The cathode, with depth bin ($d = 1$) and source-to-mask distance of B_1, is closest to the mask. It, therefore, has the smallest magnification and largest FOV. Subsequent larger depth bins will result in greater magnification and a smaller FOV. Therefore, to add the images from different depths, the image must be appropriately reformatted such that images from different depths will have the same FOV. Since no information is available outside the FOV, the frames, or edges, of the images from the depth with smaller FOV are extended with zeros, or zero padding.

The final image can be estimated by summing images over different depth bins d as follows:

$$\hat{\mathbf{F}} = \sum_{d=1}^{N_d} \mathbf{K}_{M_d} * \left[[\mathbf{O}_d \star \mathbf{G}] \otimes \mathbf{P}_{M_d} \right], \tag{3.4}$$

where $\hat{\mathbf{F}}$ is the final image estimate, $\mathbf{K}_{M_d}$ is a Kronecker delta matrix, or padding impulse function that is of size $\left[\left(C \cdot R \left(1 - \frac{M_0}{M_d} \right) + 1 \right) \times \left(C \cdot R \left(1 - \frac{M_0}{M_d} \right) + 1 \right) \right]$. The operator $(*)$ represents a convolution while $(\otimes)$ is a Kronecker multiplication operator. C is an arbitrary constant to increase the size of the matrix to avoid rounding effects, and R represents the rank of the mask. The observed pattern for a given depth index d is represented by $\mathbf{O}_d$ while $\mathbf{G}$ is the decoding matrix [19]. Therefore, $[\mathbf{O}_d \star \mathbf{G}]$ results in the reconstructed image for depth bin d. That image is then operated on by a matrix of ones ($\mathbf{P}_{M_d}$) of size $C \left[\frac{M_0}{M_d} \times \frac{M_0}{M_d} \right]$ to produce a Kronecker tensor product. Finally, summing the appropriately zero-padded arrays for all N_d depth bins will result in the depth corrected image.

To verify the accuracy of the DOI reconstruction, a collimator experiment was performed with different depths of the crystal irradiated. Figure 5 histograms the calculated cathode-to-anode ratio (CAR) versus the collimator location for three modules. The diagonal band represents the data of interest where the collimated beam interacts with the detector. A linear fit is made on the data of interest and represents the correction factor of the CAR to the true depth of interaction. The artifacts in the depth reconstruction and the fact that CAR does not have an x-intercept of 1 are still under investigation.

Figure 6 shows the experimental setup to demonstrate the improvement of using the appropriate DOI correction. There, a 63 µCi ^{57}Co source was placed $A = 99$ cm away from the mask with an offset of 45 cm from the isocenter. The detector to mask distance was set at $B_1 = 11.5$ cm.

Reconstructing the image without the use of the DOI correction results in figure 7(a), where a slight tail is visible that drags to larger x-pixel values. This is suppressed when the correction is applied, shown in figure 7(b). This is further visible in the horizontal cross-sectional sums that are shown in figure 8. The geometrically measured FWHM and the full-width-at-tenth-maximum (FWTM) values have respectively shown a 7.5% and 12.3% decrease when the DOI correction is applied and are presented in table 2. Also reported are FWHM value's 95% confidence interval of the Gaussian's fitted parameters and show that the FWHM values are not within each other's confidence interval.

2021 JINST 16 P03013

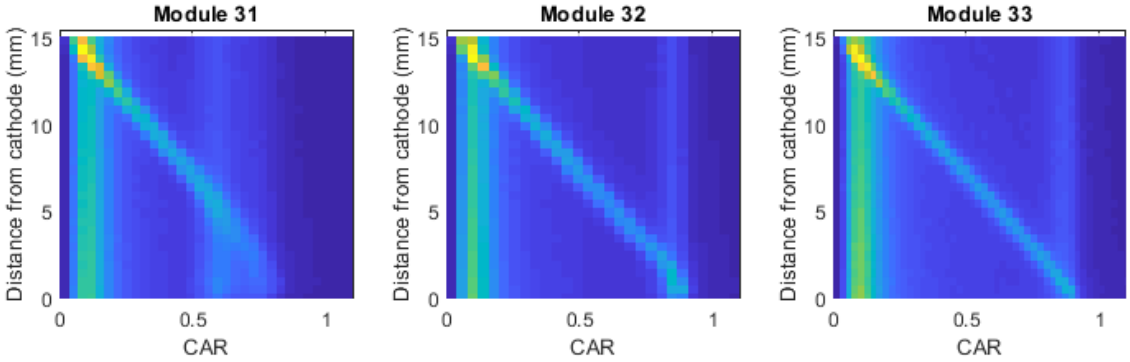

Figure 5. 2D histograms of the collimator experiment to map the cathode-to-anode ratio (CAR) to the location of the collimator for three different modules. The diagonal line that is near linear presents the relationship between the true DOI and the reconstructed depth (CAR).

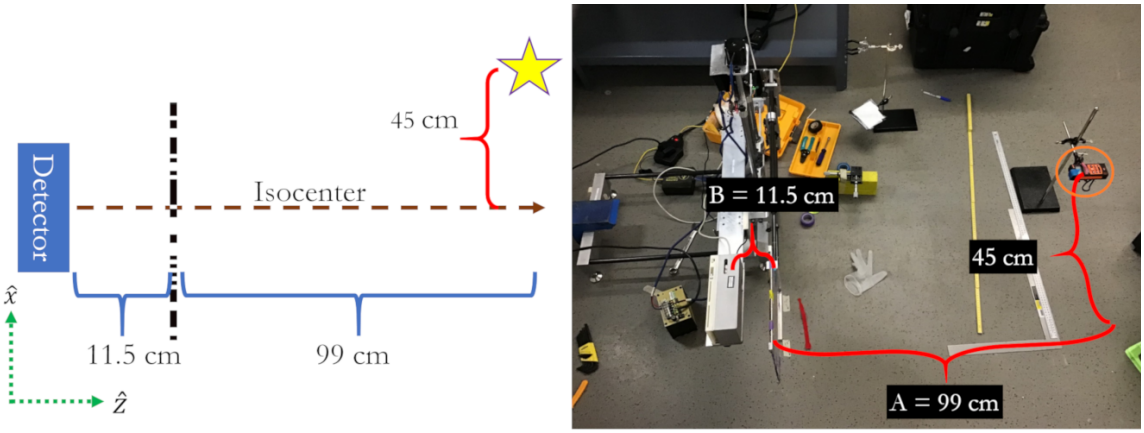

Figure 6. Experimental setup with the parameters $A = 99$ cm and $B = 11.5$ cm. The ^{57}Co source, circled in orange, was placed 45 cm off the isocenter of the detector.

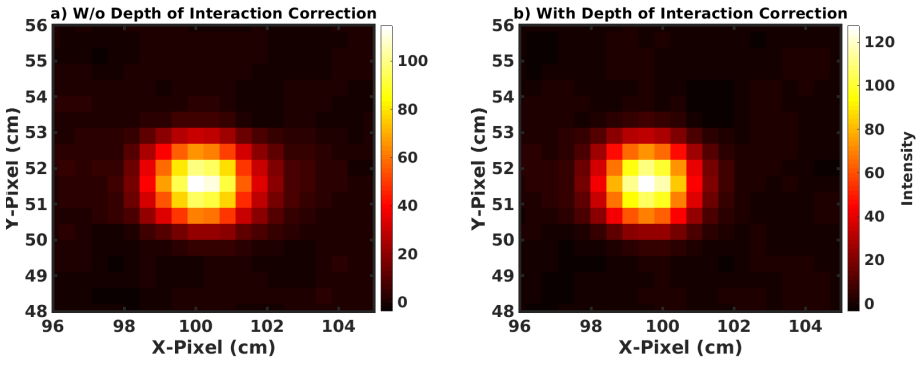

Figure 7. Reconstructed images (a) without (w/o) the use of DOI correction and (b) with DOI correction.

2021 JINST 16 P03013

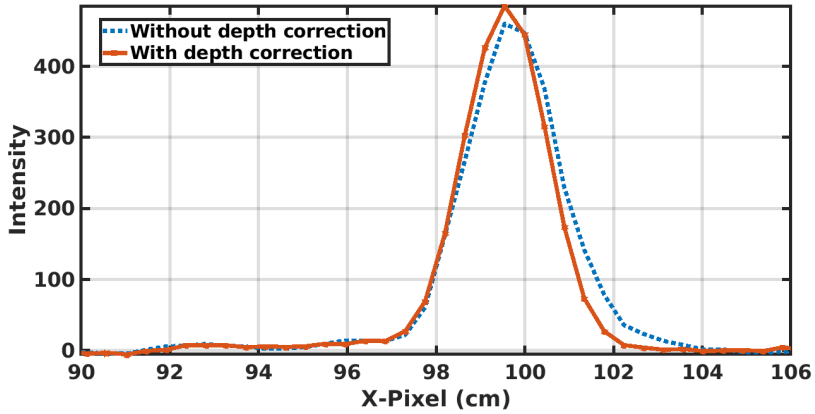

Figure 8. Horizontal cross-sections of the source's hotspot with and without applying depth correction.

Table 2. Full-width-at-half-maximum (FWHM) and full-width-at-tenth-maximum (FWTM) values for the point spread function without and with DOI correction. The values labeled with 'geometric' are calculated geometrically with linear interpolation while the 'Gaussian' values are calculated via a Gaussian fit. The margin of error values represents the 95% confidence interval on the fitted coefficient. Width values are presented in centimeters.

	FWHM (geometric)	FWTM (geometric)	FWHM (Gaussian)
Without DOI Correction	2.40	4.55	2.45 ± 0.04
With DOI Correction	2.22	3.99	2.17 ± 0.10
Percent decrease	7.5%	12.3%	12.1%

4 3D estimation of gamma-ray sources via depth refocusing

Estimation of depth in the image space, or 3D imaging, via the use of a coded aperture system has been accomplished in optical and gamma-ray cameras [6, 23–25]. Referencing (3.3), the magnification also depends on the A distance or the source-to-mask distance. If B is kept constant, the true source-to-mask distance can be deduced from investigating the magnification-focusing effects of the system during image reconstruction.

4.1 Mathematical modeling of 3D imaging using time encoded imaging

To estimate 3D source distribution, we begin with expanding the mathematical models presented in (3.1) and (3.2). In our implementation of TEI, only a portion of the mask is recorded at any given time index t since the projection of the full mask rank is larger than the detector. To record all the elements of the mask, it is raster scanned through by moving the mask horizontally and laterally as section 2.2 describes.

To build the full observation pattern $\mathbf{O}$, each measurement for a given time bin needs to be appropriately processed. The recorded observation for detector bin i (a pixel in this case) at time bin t can be modeled as

$$\mathbf{O}_{i,t} = \mathbf{F} \star \mathbf{A}^{i,t}_{A,B} \star \mathbf{D}_i + \eta, \tag{4.1}$$

2021 JINST 16 P03013

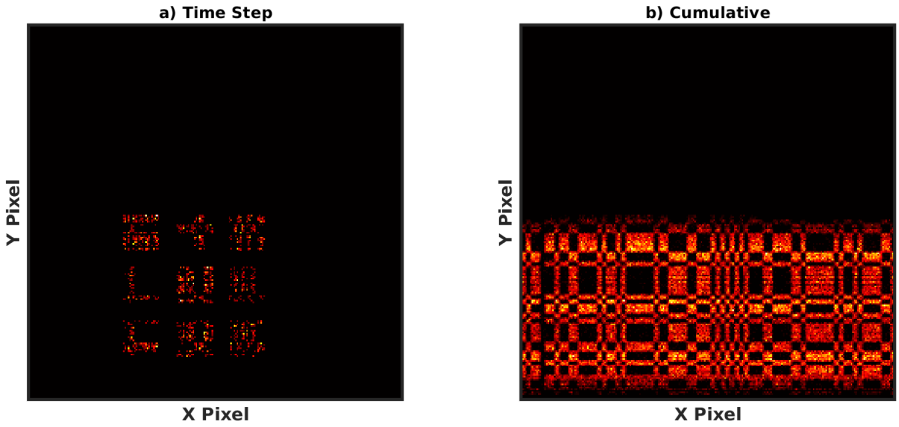

Figure 9. Projections of the observation matrix from a single point source for (a) single time index $\mathbf{O}_{\forall i,t=644}$ that has been zero padded and circularly shifted by the respective mask location.(b) presents the cumulative recorded mask from time index 1 to 644 ($\mathbf{O}_{\forall i,t=[1,644]}$). Time bin $t = 644$ was chosen as an arbitrary example to demonstrate the process.

where $(\mathbf{A}^{i,t}_{A,B})$ is the attenuation profile of the mask that encodes the source with a particular portion of the mask for that given detection and time bin with the A and B distances. $\mathbf{D}_i$ models detector effects such as efficiency compensation and any associated blurring. To sum all the observations, the pattern is first zero padded so that the size of the observed pattern matches that of the full rank or full FOV. Next, to account for the movement of the mask, the observed pattern must then be circularly shifted by an amount proportional to the physical movement of the mask in the horizontal or lateral direction. The observed pattern for pixel i at time t can be added to the full observation $\mathbf{O}$ as follows:

$$\mathbf{O} = \sum_{i=1}^{I} \text{circshift}^{i} \left[\sum_{t=1}^{T} \text{circshift}^{t}_{A,B} \left[\mathbf{P} * \mathbf{O}_{i,t} \right] \right], \tag{4.2}$$

where $\mathbf{P}$ is a Kronecker delta used to zero pad $\mathbf{O}_{i,t}$ such that $\mathbf{P} * \mathbf{O}_{i,t}$ is an array proportional in size to the rank of the mask. That array is then circularly shifted ($\text{circshift}^{t}_{A,B}[\sim]$) with respect to where the mask is located at time t and then summed over all those bins. This circshift is meant to mimic the movement of the mask. To account for the different locations of each pixel, another circshift must be applied. So the summation of the circular shifted detection bins based on the pixel locations ($\text{circshift}^{i}[\sim]$) results in an observation matrix $\mathbf{O}$, as introduced in (3.1).

Figure 9(a) visualizes a padded observation matrix $\left(\sum_{i=1}^{I} \text{circshift}^{i} \left[\mathbf{P} * \mathbf{O}_{i,t} \right] \right)$ for a single arbitrarily chosen time bin $t = 644$ out of the 79×79 total time bins for all detection bins. Figure 9(b) presents the summation of the first 644 time bins over all detection bins. It is incomplete as it only represents the first 10% of the recorded data.

Equation (4.2) shows that $\mathbf{O}$ is a function of the source-to-mask and mask-to-detector distances (A, B) and operated on by $\text{circshift}^{t}_{A,B}$. Since the mask-to-detector distance is kept constant, the global reconstructed image $\hat{\mathbf{F}}_{x,y}(A)$ is a 3 dimensional matrix that represents the spacial intensity values for a given source-to-mask (A) distance. In section 4.2, we show that the distance of the source from the mask can then be inferred by locating the most intense pixel value for each (x, y) pixel:

$$\hat{z}(x, y) = \underset{A}{\text{argmax}}\, \hat{\mathbf{F}}_{x,y}(A), \tag{4.3}$$

2021 JINST 16 P03013

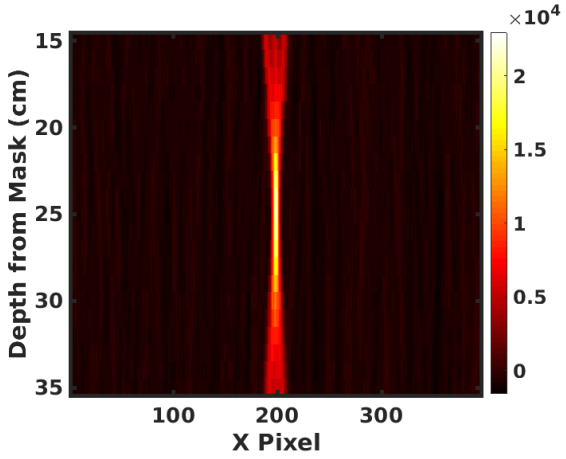

Figure 10. (a) Cross-sectional slices along the horizon of the gamma-ray image for different focal depths with the distribution peaking at $A = 25$ cm, the true source-to-mask distance. This plot presents the depth-focusing technique for a simulated gamma-ray source placed 25 cm away from the mask with a detector-to-mask distance of 30 cm.

where $\hat{z}(x, y)$ is the depth image or the distance between the estimated source location and mask. Since displaying a 3D image presents a challenge, we can plot the 2D projection of the gamma-ray image as

$$\hat{\mathbf{F}}(x, y) = \max \ \hat{\mathbf{F}}_{x,y}(A), \tag{4.4}$$

which selects the maximum pixel intensity for a given (x, y) coordinate.

4.2 3D source reconstruction of a simulated point source

Figure 10 demonstrates the depth re-focusing effect when imaging a single simulated gamma-ray source placed in the detector's isocenter, 25 cm away from the mask. It displays cross-sectional slices through the equatorial horizon of the image for the different assumed depths. There, the most intense pixel is located 25 cm from the mask, where the focal plane is equal to the true source location. Figure 11(a) demonstrates these effects for sources located in different mask-to-source distances and plots the pixel intensity. It shows a focusing and defocusing distribution with the peak near the true source depth. Therefore, we can assume that the location of the source is correlated with the most intense spot. Figure 11(b) plots the FWHM values of the distributions from (a) for the sources at different locations. It demonstrates a nearly linear trend for the distances considered.

4.3 Imaging of spatially extended special nuclear material in 3D at Idaho National Laboratory

Measurements of plutonium fuel plates were conducted at the Zero Power Physics Reactor (ZPPR) located in Idaho National Laboratory to demonstrate the depth estimation capability and eventual 3D evaluation of the source distribution. Each plate has the dimensions of $7.62 \times 5.08 \times 0.3175$ cm^3 with the main elemental composition of the plates including ~75% ^{239}Pu and ~22% ^{240}Pu, for a total mass of ~111 g [26].

2021 JINST 16 P03013

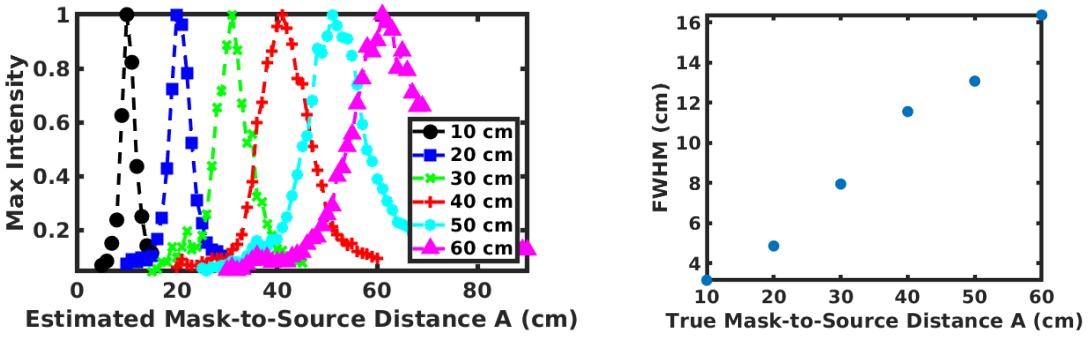

Figure 11. (a) Pixel intensity profile for simulated sources at different depths from the detector using the depth-focusing technique. (b) FWHM values of the estimated depth-intensity curves for the different source locations.

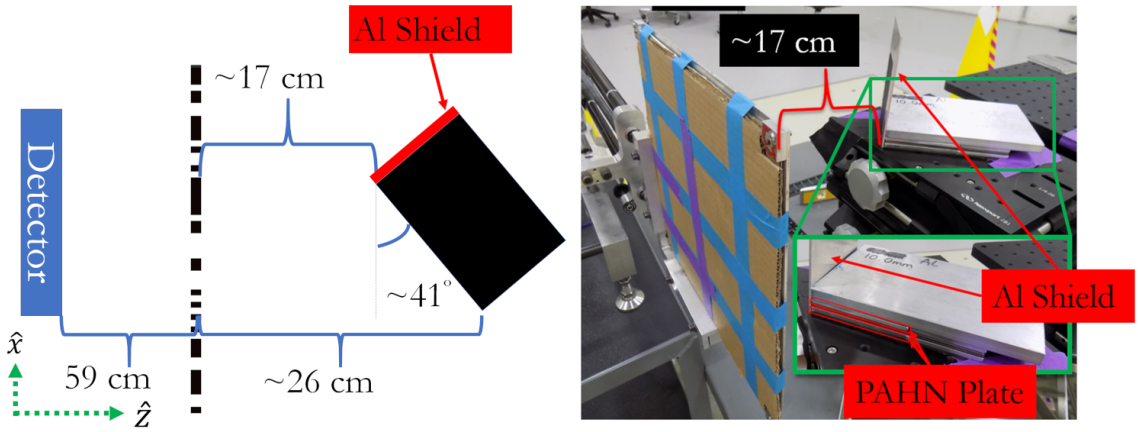

Figure 12. (a) Diagram of the experimental setup at INL. (b) Optical images of the setup with an inset image zooming into the setup of the plates.

In the experimental setup, two plates were sandwiched together with a 2.9 mm carbon steel plate in between them. The top and bottom of the Pu plates were covered with aluminum. Figure 12(a) shows a diagram of the experimental setup and presents the plutonium plates angled ~41° away from the detector plane with the closest point of the plate ~17 cm away from the mask. The 5.08 cm face was shielded with a 2 mm aluminum plate, as shown in the inset of figure 12(b). The measurement values are reported as approximations due to the authors' inability to complete the measurements themselves.

Figure 13 plots the spectrum for the 1 hour measurement. The image reconstruction used the 59.5 keV from ^{241}Am as well as the 99 and 103 keV peaks that are also predominantly from ^{241}Am among other Plutonium emissions [27]. The total number of counts that are used in the following images is almost 10 million.

The reconstructed gamma-ray images are available in the left column of figure 14 with figure 14(a) showing the raw gamma-ray image ($\hat{\mathbf{F}}(x, y)$ from (4.4)) while figure 14(b) applies an intensity cut of 125. The right column of figure 14 plots the depth images, ($\hat{z}(x, y)$ from (4.3)), as estimated by the depth-refocusing technique. Figure 14(c) plots the raw depth image of all the

2021 JINST 16 P03013

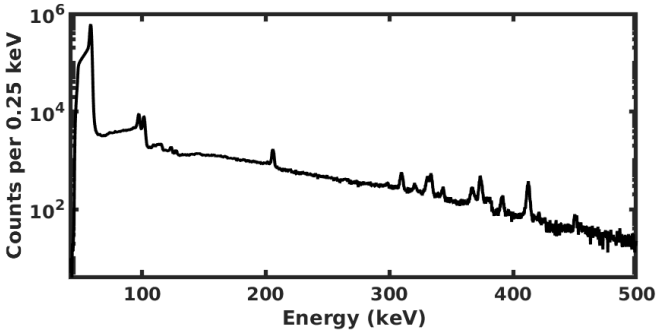

Figure 13. The recorded gamma-ray spectrum of the plutonium plates measured at INL. Note that there is a sharp decline at the low energy range due to the readout threshold.

available pixels while figure 14(d) presents the depth estimate with the intensity cut mask used in (b). The range of depths utilized in the reconstruction ranged from 15 to 27 cm with increments of 0.1 cm. In the depth images, a clear gradient along the plates is visible indicating the source is distributed in 3-dimensions rather than in a single depth plane.

We apply a linear fit along the plate's profile in the depth image for the top and bottom plate separately. The edges were chosen from the image with the intensity cut which we defined to be the boundaries of the plates. Next, the response was averaged along the height of the plates for 0.8 cm, which is the thickness of the plate.

The angles of the plates are estimated from the slopes of the linear fit. They are 49.0° ± 1.2 and 48.2° ± 1.8 for the top and bottom plates respectively, which is an overestimation of the ~41° measured physically during the experiment. Once again, the margin of error presents the 95% confidence interval of the regressed slopes. The coefficient of determination (R^2) values for the linear fits are 0.84 and 0.74 for the top and bottom plate respectively.

4.4 Discussion

Defocused artifacts possibly present the largest contributor to the depth estimation error [24]. The artifacts arise from sources in different planes that contribute to the reconstruction plane and therefore bias the depth estimation. This is first visible in figure 11(a) that plots the different pixel intensity along the reconstructed depths. One would expect the distribution to resemble a delta function had there been no defocused bias effects. Figure 15 reconstructs images of a simulated source located 30 cm away from the mask with the assumed reconstruction plane of (a) 10, (b) 30, or (c) 50 cm. Naturally, the in-focus image (b) presents the best result but when a different reconstruction plane is assumed, such as in (a) or (c), the reconstructed images are corrupted and exhibit hotspot multiplication.

The use of maximum-likelihood expectation-maximization (MLEM) will perhaps result in an improved estimate as cross-correlation for each depth plane may not be sufficient to account for additional effects that could be modeled in the system response. It will attempt to reconstruct the source distribution with the highest likelihood and will result in a lower biased estimation. Next, as suggested by Chang et al. [28], a more carefully chosen mask could suppress the properties of defocused artifacts. They suggest that random mask arrays have superior tomographic abilities

2021 JINST 16 P03013

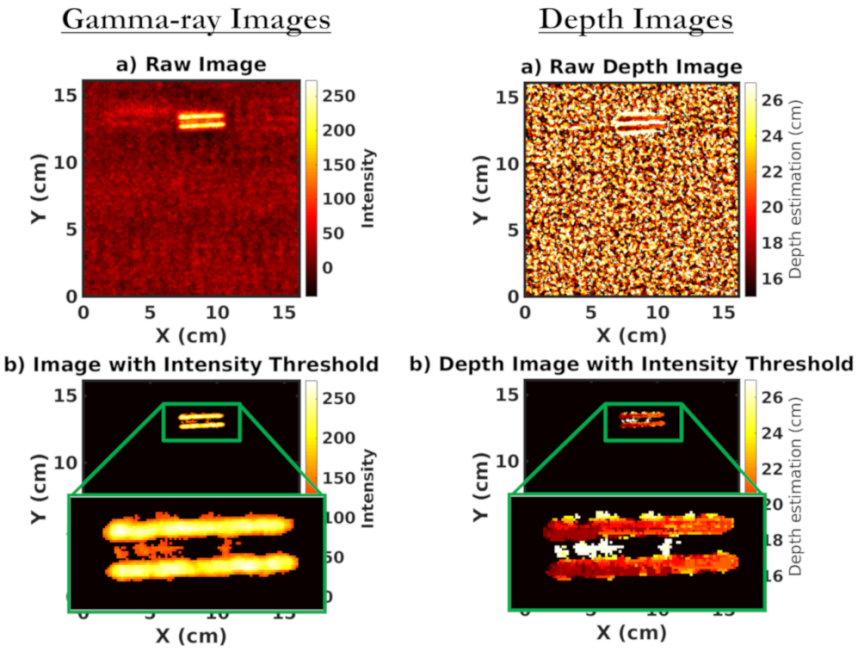

Figure 14. The left column presents the reconstructed gamma-ray images with (a) the raw gamma-ray image and (b) image with the intensity cut. The right column presents the depth images, or the estimated source to mask distance with (c) the raw image and (d) with the intensity cut mask utilized in (b) of this figure.

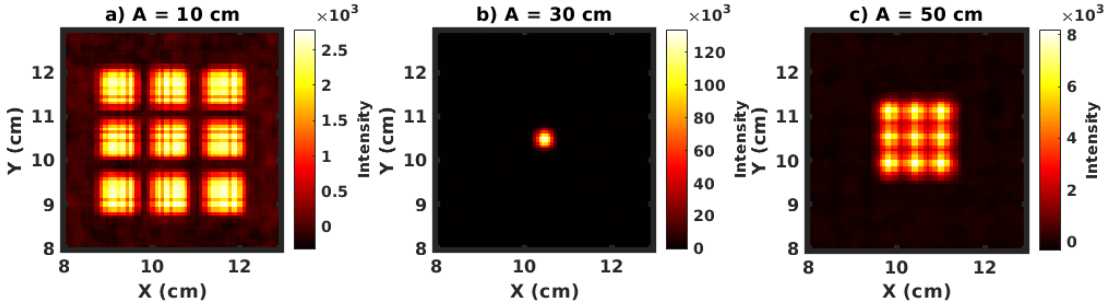

Figure 15. Reconstructed images of a simulated single point source located $A = 30$ cm away from the mask and a mask-to-detector distance of $B = 30$ cm. The sub-figures present images using different reconstruction planes with a source-to-mask distance of (a) 10, (b) 30, or (c) 50 cm. The figure presents the depth-focusing effects and associated defocused artifacts. The multiplied hotspot artifacts are associated with the 3×3 detector array.

when compared to non-redundant arrays as the mask's randomness will reduce the defocused reconstructed structure. Artifacts in figure 15(a) and (c) give examples of the defocused structure.

The use of the depth-refocusing technique can assist with qualitative analysis of the objects as well as spatial quantitative estimation of the radioactive material, for applications such as holdup in pipes. As plutonium is very dense and highly attenuating to gamma rays, the technique will not be able to deduce the extent of the source beyond the superficial face of the material. In addition, any attenuating material will also skew the results and will need to be accounted for in

2021 JINST 16 P03013

the system response. Therefore, higher energy gamma rays, high intensity radiographic, or neutron tomographic techniques will be more informative in those scenarios.

5 Conclusion

Application of subpixel estimation allows the CdZnTe imaging system to achieve a better than 0.6 cm FWHM for an (A = 71 cm, B = 30 cm) configuration when imaging two ^{57}Co sources placed 1 cm apart. Note that the FWHM value also includes the extent of the check source, which the manufacturer lists as about 0.5 mm. The use of subpixel estimation improves the resolution by almost 10% for the given source configuration. The performance could be refined with the application of MLEM but was not explored in this study due to the difficulty associated with determining a mathematically justified stopping criteria.

With the application of the proposed 3D imaging technique, the 3D distribution of spatially extended special nuclear material has been estimated using time-encoded imaging. For experimental measurements of plates angled ~41° away from the image plane, the estimated angle from the depth-refocusing technique reconstructed the out of plane angles of the SNM plates with 20% and 18% error.

Acknowledgments

The authors would like to thank their current and past colleagues of the Orion Radiation Measurement Group whose work they leverage, specifically the work of Dr. Steven Brown. We also thank Mr. Brendan Huhlein and the staff at INL for their support in the measurement campaign.

This work was supported by the Department of Energy NA-22 office, the Consortium for Verification Technology under grant DE-NA002131, and the Consortium for Monitoring, Technology, and Verification through award No. DE-NA0003920. The views and opinions of the authors expressed do not necessarily state or reflect those of the U.S. Government or any agency thereof.

References

[1] E. Caroli, J.B. Stephen, G. Di Cocco, L. Natalucci and A. Spizzichino, *Coded aperture imaging in x- and gamma-ray astronomy*, *Space Sci. Rev.* **45** (1987) 349.

[2] R. Accorsi, F. Gasparini and R.C. Lanza, *A coded aperture for high-resolution nuclear medicine planar imaging with a conventional anger camera: experimental results*, *IEEE Trans. Nucl. Sci.* **48** (2001) 2411.

[3] L.J. Mitchell et al., *Mobile imaging and Spectroscopic Threat Identification (MISTI): System overview*, in proceedings of the *2009 IEEE Nuclear Science Symposium Conference Record (NSS/MIC)*, Orlando, FL, U.S.A., 24 October–1 November 2009, pp. 110–118.

[4] S.J. Kaye, W.R. Kaye and Z. He, *Experimental Demonstration of Coded Aperture Imaging Using Thick 3D-Position-Sensitive CdZnTe Detectors*, in proceedings of the *2009 IEEE Nuclear Science Symposium Conference Record (NSS/MIC)*, Orlando, FL, U.S.A., 24 October–1 November 2009, pp. 1902–1906.

[5] K.F. Koral, W.L. Rogers and G.F. Knoll, *Digital Tomographic Imaging with Time-Modulated Pseudorandom Coded Aperture and Anger Camera*, *J. Nucl. Med.* **16** (1975) 402.

2021 JINST 16 P03013

[6] S.T. Brown, D. Goodman, J. Chu, B. Williams, M.R. Williamson and Z. He, *Time-Encoded Gamma-Ray Imaging Using a 3-D Position-Sensitive CdZnTe Detector Array*, *IEEE Trans. Nucl. Sci.* **67** (2020) 464.

[7] J.G.M. FitzGerald, L.W. Burggraf, B.R. Kowash and E.L. Hull, *A modulating liquid collimator for coded aperture adaptive imaging of gamma-rays*, *IEEE Trans. Nucl. Sci.* **60** (2013) 2300.

[8] J. Brennan et al., *Source detection at* 100 *meter standoff with a time-encoded imaging system*, *Nucl. Instrum. Meth. A* **877** (2018) 375 [arXiv:1706.04230].

[9] K. Koral, J. Freitas, W. Rogers and J. Keyes, *Thyroid scintigraphy with time-coded aperture*, *J. Nucl. Med.* **20** (1979) 345.

[10] P.A. Russo, *Gamma-Ray Measurements of Holdup Plant-Wide: Application Guide for Portable, Generalized Approach*, LA-14206 (2005).

[11] N. Rebei, M. Fang and A. Di Fulvio, *Quantitative and three-dimensional assessment of holdup material*, *Nucl. Instrum. Meth. A* **984** (2020) 164630.

[12] Z. Chen, Y. Zhu and Z. He, *Intrinsic photopeak efficiency measurement and simulation for pixelated CdZnTe detector*, *Nucl. Instrum. Meth. A* **980** (2020) 164501.

[13] Y. Zhu and Z. He, *Performance of Larger-Volume* $40 \times 40 \times 10$ *and* $40 \times 40 \times 15\,mm^3$ *CdZnTe Detectors*, *IEEE Trans. Nucl. Sci.* **68** (2021) 250.

[14] Z. He, *Review of the Shockley-Ramo theorem and its application in semiconductor gamma-ray detectors*, *Nucl. Instrum. Meth. A* **463** (2001) 250.

[15] W.R. Kaye, *Energy and Position Reconstruction in Pixelated CdZnTe Detectors*, Ph.D. Thesis, University of Michigan, Ann Arbor MI U.S.A. (2012).

[16] Y. Zhu, S.E. Anderson and Z. He, *Sub-pixel position sensing for pixelated, 3-D position sensitive, wide band-gap, semiconductor, gamma-ray detectors*, *IEEE Trans. Nucl. Sci.* **58** (2011) 1400.

[17] W.K. Warburton, *An Approach to Sub-Pixel Spatial Resolution in Room Temperature X-Ray Detector Arrays with Good Energy Resolution*, *MRS Online Proc. Libr.* **487** (1997) 531.

[18] Y. Zhu, *Digital Signal Processing Methods for Pixelated 3-D Position Sensitive Room-Temperature Semiconductor Detectors*, Ph.D. Thesis, University of Michigan, Ann Arbor MI U.S.A. (2012).

[19] E.E. Fenimore and T.M. Cannon, *Coded aperture imaging with uniformly redundant arrays*, *Appl. Opt.* **17** (1978) 337.

[20] S. Brown, *Time-Encoded Thermal Neutron Imaging UsingLarge-Volume Pixelated CdZnTe Detectors*, Ph.D. Thesis, University of Michigan, Ann Arbor MI U.S.A. (2017).

[21] K. Ziock and M. Blackston, *Real time depth-of-interaction correction for coded-aperture, gamma-ray images*, *Nucl. Instrum. Meth. A* **916** (2019) 56.

[22] Eckert & Ziegler Strahlen- und Medizintechnik AG, *Overview — point sources*, (2017) https://www.ezag.com/home/products/isotope_products/isotrak_calibration_sources/reference_sources/gamma_sources/point_sources/.

[23] A. Levin, R. Fergus, F. Durand and W. Freeman, *Image and depth from a conventional camera with a coded aperture*, *ACM Trans. Graph.* **26** (2007) 70.

[24] T.M. Cannon and E.E. Fenimore, *Tomographical imaging using uniformly redundant arrays*, *Appl. Opt.* **18** (1979) 1052.

2021 JINST 16 P03013

[25] R. Accorsi, *Design of Near-Field Coded Aperture Cameras for High-Resolution Medical and Industrial Gamma-Ray Imaging*, Ph.D. Thesis, Massachusetts Institute of Technology, Cambridge MA U.S.A. (2001).

[26] A.D. Fulvio et al., *Passive Assay of Plutonium Metal Plates Using a Fast-Neutron Multiplicity Counter*, *Nucl. Instrum. Meth. A* **855** (2017) 92.

[27] D. Reilly, N. Ensslin, H.J. Smith and S. Kreiner, *Passive Nondestructive Assay of Nuclear Materials*, NUREG/CR-5550 (1991).

[28] L.-T. Chang, B. Macdonald and V. Perez-Mendez, *Comparisons Of Coded Aperture Imaging Using Various Apertures And Decoding Methods*, *Proc. SPIE* **0089** (1977) 9.

[29] K.P. Ziock et al., *Large Area Imaging Detector for Long-Range, Passive Detection of Fissile Material*, *IEEE Trans. Nucl. Sci.* **51** (2004) 2238.

2021 JINST 16 P03013